Investigation of the physico-chemical properties of Ni-Mg-Al-La catalysts from ultrasound-assisted synthesis

Hamed Kalawoun, Carmen Ciotonea, M. Marinova, Cédric Gennequin, François Delattre

Ultrasonics Sonochemistry 104 (2024) 106806

Contents lists available at ScienceDirect

Ultrasonics Sonochemistry

journal homepage: www.elsevier.com/locate/ultson

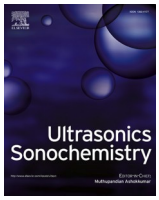

Investigation of the physico-chemical properties of Ni-Mg-Al-La catalysts from ultrasound-assisted synthesis

H. Kalawoun [a], C. Ciotonea [a], M. Marinova [b], C. Gennequin [a], F. Delattre [a,*]

[a] Unité de Chimie Environnementale et Interactions sur le Vivant UCEIV), UR 4492, Université du Littoral-Côte d'Opale, 59140 Dunkerque, France
[b] Unité Matériaux et Transformations (UMET), UMR 8207, Institut Michel-Eugène Chevreul, Université de Lille, 59000 Lille, France

ARTICLE INFO

Keywords:
Layered double hydroxides synthesis
Ni-Mg-Al-La catalysts
Ultrasonic synthesis
Mixed oxides
Lanthanum insertion

ABSTRACT

This work reports on the ultrasonic synthesis of layered double hydroxides (LDH), also known as hydrotalcite-type materials. We have studied the influence of ultrasonic irradiation parameters (power, time, temperature) on the physicochemical properties of $Ni_2Mg_4Al_{1.8}La_{0.2}$ hydrotalcite-type precursors and related mixed oxides (MO). The low-frequency acoustic cavitation (22 kHz) was applied during the precipitation and aging steps of co-precipitation synthesis and the results were compared to the classical preparation route. The materials were characterized by ATR-FTIR, XRD, N_2 adsorption–desorption, SEM-EDX, S/TEM-HAADF, and XPS. Using the combination of acoustic cavitation-assisted precipitation and aging steps, XRD experiments show a higher purity hydrotalcite phase and a better incorporation of lanthanum ions into the LDH structure. As expected, morphological characterization shows a reduction in average crystallite size and an increase in surface area and pore volume, combined with a drastic reduction in synthesis time (45 min at room temperature versus 19 h at 60 °C in conventional synthesis). The insertion of a larger quantity of La is observed by S/TEM-EDSX mapping which also shows a better distribution of lanthanum atoms within the LDH and mixed oxide structures.

1. Introduction

Among several classes of lamellar-like materials, layered double hydroxides (LDHs), also known as hydrotalcite-like compounds or anionic clays, have attracted much attention in recent years due to their versatility, ease of synthesis, flexible composition, high chemical, and thermal stability, etc. [1]. LDHs are used for widespread applications in different fields including adsorption [2], CO_2 capture [3], drug delivery [4], heterogeneous catalysis [5], fire retardant additives [6], wastewater treatment [7], etc. A part of these applications are included in environmental remediation, such as the adsorption of CO_2, wastewater treatment, and valorization of greenhouse gases into other high-value molecules such as synthetic fuels or chemicals [8].

LDHs are constituted of several layers containing cations also known as brucite-like layers, separated by an interlayer space containing anionic species [9]. The general formula of LDHs is: $[M^{II+}_{1-x}M^{III+}_{x}(OH)_2][A^{n-}_{x/n}].yH_2O$, where M^{II+}/M^{III+} are divalent and trivalent metal ions and A^{n-} a hydrated anion. In addition, x represents the mole fraction of the trivalent cation and y the degree of hydration. In the position of M^{II+} can be found Mg^{2+}, Ni^{2+}, Co^{2+}, Zn^{2+}, Cu^{2+}, while for M^{III+} are present usually Al^{3+}, Ce^{3+}, Fe^{3+}, Mn^{3+}, Cr^{3+} and in the place of A^{n-} may be found CO_3^{2-} or NO^{3-} [10]. These materials can be used as they are in many applications. In catalysis, the LDHs are used as precursors for the generation of mixed oxides, obtained after a thermal treatment. One of the high values of using the LDHs is the high metal loading in the case of monometallic or multi-metallic compositions with high dispersions by comparison to supported catalysts that have limited metal loadings. The mixed oxides derived from LDHs are characterized by a homogeneous composition and expose good properties such as high surface area, small crystallite size, and acid/base balance [11]. The synthesis of LDHs can be achieved by using several methods like co-precipitation, urea hydrolysis, sol–gel, ion exchange, spontaneous combustion, hydrothermal treatment, or mechanochemical synthesis [12,13]. Nevertheless, these preparation methods require complex synthesis steps and long periods and most of them result in heterogeneous composition of the oxide phases. To prepare materials with enhanced physicochemical properties, new compositions, and morphologies have been explored in recent years. The co-precipitation is by far one of the most used methods for LDH synthesis. In the first step, the aqueous solutions of bivalent and trivalent metal salts are added dropwise to the carbonate-based solution to form a stack of layers of cations and interlamellar spaces containing the mobile and interchangeable anions. To carefully obtain such

* Corresponding author.
E-mail address: delattre@univ-littoral.fr (F. Delattre).

https://doi.org/10.1016/j.ultsonch.2024.106806
Received 24 November 2023; Received in revised form 2 February 2024; Accepted 8 February 2024
Available online 13 February 2024

structures, this step must be done very slowly by the addition dropwise of the precursors. The second step of co-precipitation consists of an ageing process which takes place currently in an oven for a minimum of 18 h [14,15]. Although this synthesis method is simple and economical, it does not allow perfect control of particle and aggregate tailoring. Therefore, other alternative synthesis methods which are using ultrasounds have been developed [16,17]. It has been demonstrated that acoustic cavitation accelerates crystal nucleation and formation, and reduces the agglomeration of the particles. The smaller nanoparticles formed induce an increase in the specific surface area [18,19]. In addition, materials derived from ultrasound-assisted synthesis (UAS) have been shown to deliver improved performance, particularly in hydrogen production, adsorption of gaseous and aqueous pollutants, and environmental applications [20–22].

In this work, we have studied the influence of varying ultrasonic irradiation parameters on the physicochemical properties of $Ni_2Mg_4Al_{1.8}La_{0.2}$ hydrotalcite precursors to produce mixed oxides to be used as catalysts for the production of energy molecules by processes like dry reforming of methane, glycerol or ethanol steam reforming and partial oxidation of methane [23–26]. Nickel (Ni) is one of the most widely metals used as the active phase in several catalytic applications. Nevertheless, it is a cheap and abundant metal in comparison to noble metals (Pt, Rh, Ru, and Ir) [27]. Moreover, it has been demonstrated that rare-earth elements, such as lanthanum or cerium, improve the activity and stability of mixed oxides issued from the calcination of LDH precursors. Several works have shown that the addition of lanthanum improves catalyst stability, contributes to improved metal dispersion, and promotes the adsorption of CO_2 molecules. Lanthanum oxide acts as an oxygen reservoir, facilitating the removal of deposited coke [28]. These results have been observed when La_2O_3 is used as a support modifier. In the case of LDHs, a few studies have shown the effect of adding lanthanum on the activity and stability of these materials in the dry reforming of methane. The results showed that lanthanum incorporation increases low and medium basicity, improves the reducibility of active species, and contributes to the gasification of deposited carbon [29,30]. However, the problem regularly encountered is the difficulty of total insertion of these cations within the LDH structures. This reduces the benefits of adding these promoter elements and is a reverse consequence in the case of the presence of excess cations outside the lamellar structure. Thus, one of the key points that will be evaluated is the insertion of lanthanum in brucite-like layers using ultrasounds, since the application of acoustic cavitation has already demonstrated its ability to enhance the insertion of cerium ions into hydrotalcite structure [31]. The stoichiometric ratio of lanthanum in $Ni_2Mg_4Al_{1.8}La_{0.2}$ hydrotalcite precursor has been chosen to obtain a weight percentage of 4.45 wt% of lanthanum, which corresponds to the optimal value regarding those reported in the literature [23,32]. To determine the optimum synthesis conditions, the effect of the various ultrasonic experiment parameters (power density, time, and temperature) on the physicochemical properties of $Ni_2Mg_4Al_{1.8}La_{0.2}$ is evaluated. These materials were compared with a reference material of the same composition prepared by the conventional co-precipitation method.

2. Experimental section

2.1. Precursor and mixed oxide preparations

2.1.1. $Ni_2Mg_4Al_{1.8}La_{0.2}$ LDH synthesis via conventional co-precipitation method (Input A, Table 1)

An aqueous solution was prepared by dissolving 4.26 g of Ni $(NO_3)_2{\cdot}6H_2O$ (AlfaAesar, wt.98 %), 7.44 g of $Mg(NO_3)_2{\cdot}6H_2O$ (Acros Organics, wt.99 %), 4.92 g of $Al(NO_3)_3{\cdot}9H_2O$ (Chem-Lab, wt.98.5 %) and 0.62 g of $La(NO_3)_3{\cdot}_9H_2O$ (AlfaAesar, wt.99.9 %) in 50 mL of demineralized water. This solution was added dropwise under vigorous stirring to 100 mL constituted from 15 mL of an aqueous solution of Na_2CO_3 (Acros Organics, wt.99.5 %) (1 M) and 85 mL of demineralized water. The pH was maintained between 9.5 and 10 by adding an aqueous solution of NaOH (ACS, wt.98 %) (2 M). The synthesis was performed at 60 °C under stirring for 45 min. The resulting slurry was aged in an oven at 60 °C for 18 h. Then, the precipitate was filtered and washed several times with hot demineralized water (60 °C) until neutral pH followed by drying at 60 °C for 48 h. The obtained LDH material was ground to give fine powders. The mixed oxides are then obtained by calcination of LDH materials in a muffle furnace at 800 °C for 4 h, by using a ramp of 1 °C.min^{-1}.

Table 1
Applied conditions and employed strategy to optimize the preparation protocol.

Input	Temp. (°C)	Power density (W. L^{-1})	Precipitation step (Mode, time)	Aging step (Mode, time)
A	60	–	silent, 45 min	silent, 18 h
B	60	360	US, 45 min	silent, 18 h
C	60	360	US, 45 min	US, 30 min
D	60	360	US, 15 min	US, 30 min
E	20	360	US, 15 min	US, 30 min
F	20	180	US, 15 min	US, 30 min
G	20	90	US, 15 min	US, 30 min

2.1.2. $Ni_2Mg_4Al_{1.8}La_{0.2}$ LDH synthesis via ultrasonic-assisted co-precipitation method (Inputs B-G, Table 1)

The sonication was carried out using an Ultrasonic Lab750 SinapTec apparatus (22 kHz). This system consists of a pipe surrounded by eight transducers, each with a maximum power of 50 W. To control system temperature, the whole system is cooled by a network of glycol fluid surrounding the pipe and transducers. Catalyst preparation was carried out in a reactor containing 100 mL of aqueous Na_2CO_3 solution (1 M) and immersed inside the pipe. Stirring is provided by a mini magnetic stirrer placed in the pipe beneath the reactor.

2.1.3. Experimental methodology

For the synthesis of $Ni_2Mg_4Al_{1.8}La_{0.2}$ LDH under ultrasounds, a solution of precursors with the same concentration as for classical protocol was prepared. The different experimental conditions used during the synthesis under ultrasounds are summarized in Table 1 and include temperature, power density, and the effect of duration of mixing and aging steps. Our strategy was to evaluate the effects of the different conditions on the physicochemical properties of materials (inputs B to G). To do this, they were compared to the reference synthesis in silent mode (input A). First, we introduced ultrasonic irradiation only for the mixing step (input B) with the same duration as the reference synthesis, and then we subjected the sample to ultrasound for the aging step (input C). From entry D to G, all experiments focus on the total synthesis of LDH materials under ultrasonic irradiations to study the effect of irradiation time (input D), temperature (input E), and power density (inputs F and G).

2.2. Characterization

After the preparation the LDHs and the mixed oxides were characterized by X-ray diffraction (XRD), attenuated total reflectance, Fourier transform infrared (ATR-FTIR) spectroscopy, N_2 physisorption, scanning electron microscopy coupled to energy-dispersive X-ray spectroscopy (SEM-EDX), scanning transmission electron microscopy coupled to energy-dispersive X-ray spectroscopy (S/TEM-EDXS), and by X-ray photoelectron spectroscopy (XPS) to investigate the structural, textural and morphological properties of LDHs materials and derived mixed oxides.

XRD patterns were studied using a Bruker D8 Advance diffractometer equipped with a copper anode ($\lambda = 1.5406$ Å). The scattering intensities were measured over an angular range of $5° < 2\theta < 80°$ for LDH materials and of $22° < 2\theta < 80°$ for mixed oxides with a step size of $2\theta = 0.02°$ and

a count time of 2 s per step. The diffraction peaks have been indexed by comparison with the joint committee on powder diffraction standards (JCPDS) files by using EVA software. The average Crystallite sizes (ACS) of the LDH materials were calculated using the Scherrer equation:

$$ACS = \frac{K \times \lambda}{\beta \times cos\theta}$$

Where K is the dimensionless shape factor (0.9), λ is the X-ray wavelength used (1.5406 Å), β is the line broadening at half the maximum intensity (FWHM) of the (0 0 3) diffraction peak and θ is the Bragg angle.

The ATR-FTIR spectra of precursors were recorded on a PerkinElmer Spectrum BXII spectrometer over the wavenumber range of 500–4000 cm^{-1} with a resolution of 2 cm^{-1}.

The textural properties of mixed oxides were analyzed by nitrogen physisorption at −196 °C (Micrometrics, 3Flex Physisorption, then textural properties were calculated from the adsorption/desorption isotherms by using the Microactive 4.06 software). The mixed oxide powders (200 mg) have been previously degassed under vacuum at 350 °C for 4 h to eliminate the impurities. Specific surface area was calculated using the BET algorithm, in the P/P_0 of 0.10 to 0.25, pore volume is determined at $P/P_0 = 0.98$, on the adsorption branch. In addition, the specific surface area of layered double hydroxides was determined by using the same process of physisorption in the Thermoelectron Qsurf M1 device. Before analysis, 35 mg of LDH material must undergo a degassing step during which impurities and any organic compounds or water vapor are removed from the surface of the material by heating. This step takes place at a temperature of 55 °C for 45 min.

Scanning electron microscopy (SEM) was performed on the LDHs materials and correspondent mixed oxides by using JEOL ™ JSM7100F apparatus coupled with Energy-dispersive X-ray spectroscopy (EDX). This machine is equipped with three ultrathin windows (30 mm^2) energy-dispersive X-ray detectors (Bruker ™ XFlash 6/30). Spectral acquisitions were performed at 15 kV, 145 pA. Before each experiment, samples were coated with a 10 nm chromium layer (Quorum ™ Q150T ES sample preparation system).

The morphology of LDHs materials was performed in a TITAN Themis 300 S/TEM equipped with a high brightness Schottky field emission gun, a monochromator, and a probe aberration corrector allowing an energy and resolution of 150 meV and 70 pm, respectively. The microscope is equipped with several annular dark field detectors and a super-X detector system with four windowless silicon drift detectors for electron dispersive X-ray spectroscopy (EDXS). The experiments were performed at 300 kV with a semi-convergence angle of about 20 mrad, probe size of the order of 500 pm, and probe current between 60 and 100 pA. For high-angle annular dark field (HAADF), the images were collected with angles between 50 and 200 mrad. EDS mapping was performed in spectrum imaging mode with a dwell time per pixel of about 15 μm and continuously scanning frames until a total acquisition time of about 15 to 20 min.

The XP spectroscopy (XPS) analyses of LDH materials were performed on a Kratos Analytical Axis Ultra DLD spectrometer, equipped with a monochromatic Al Kα X-ray source (1486.6 eV) operating at 225 W (15 kV, 15 mA). The charge neutralizer system was used for all acquisitions and a Pass Energy of 20 eV and a step size of 0.05 eV. Fresh samples were analyzed under ultra-high vacuum with an instrument base pressure of 5.10^{-10} torr. Binding energies (BE) were referenced to the unresolved Si 2p doublet for SBA-15 positioned at 103.5 eV.

3. Results and discussion

3.1. Chemical characterization

3.1.1. X-ray diffraction analysis

To assess LDHs formation and mixed oxide crystalline phase materials, X-ray diffractograms of hydrotalcite samples and the corresponding mixed oxides from conventional synthesis (input A) and ultrasound-assisted synthesis (UAS) (input E) are compared in Fig. 1 (other results are presented in Fig. S1). The XRD patterns are compared with JCPDS file No. 22–0700 of $Mg_6Al_2CO_3(OH)_{16}{\cdot}4H_2O$, which confirms the presence of LDHs phases for all solids [33]. However, when the conventional method is used, the presence of a certain impurity corresponding to $LaCO_3OH$ is noted, these almost disappear after the ultrasound-assisted synthesis (JCPDS: 49–0981). The residual presence of lanthanum hydroxycarbonate shows that in the case of conventional synthesis, some of the lanthanum is not inserted into the nanosheets, notably due to its large ionic radius and lower electronegativity than that of other ions [23]. Otherwise, it is remarkable to note that the intensity of peaks related to the impurities became less intense or disappeared by applying ultrasounds (Fig. 1 and Fig. S1). This could be attributed to better incorporation of lanthanum ions into the hydrotalcite structure under ultrasound.

To support the hypothesis of insertion of lanthanum, unit cell parameters were calculated to assess and confirm the possibility of significant cation incorporation into the hydrotalcite structure which is characterized by a rhombohedral symmetry. The parameter “a” corresponds to the average distance between two metal ions of the laminar structure, while the parameter “c” corresponds to the interlayer distance. The parameter “a” has been calculated from the first peak in the doublet at approximately $2\theta = 61°$ by using this relationship: $a = 2 \times d_{(1\,1\,0)}$. The parameter “c” is calculated from the position of the first peak ($2\theta = 11°$) according to $c = 3 \times d_{(0\,0\,3)}$ [34]. The lattice parameters of the hydrotalcite sample prepared by the conventional coprecipitation method (input A) and the sample prepared by ultrasounds under different conditions (inputs B to G) as well as $Ni_2Mg_4Al_2$ are listed in Table 2.

As shown in Table 2, the samples prepared under acoustic cavitation (inputs B to G) are characterized by higher lattice parameters than the ones obtained using the conventional method (Table 2). The highest values are obtained for sample E at room temperature and with a precipitation step of only 15 min. This finding shows that the efficiency of ultrasound synthesis does not depend on temperature. However, reducing ultrasonic power tends to reduce unit cell parameters (Inputs F and G).

Thus, the relatively large increase in the c parameter during ultrasound syntheses is consistent with the possible incorporation of lanthanum. Indeed, a 0.049 nm increase in the parameter can be seen when comparing samples, A and E, respectively. Knowing La^{3+} has a large ionic radius in comparison to the other ions (0.116 nm (La^{3+}) > 0.069 nm (Ni^{2+}), 0.072 nm (Mg^{2+}), 0.054 nm (Al^{3+})), the observed differences of c parameter are consistent with the better insertion of lanthanum under ultrasonic-assisted synthesis [39]. As a result, the increase in the parameter “a” is related to the expansion of the distance cation-cation in the brucite layer resulting from lanthanum insertion. At the same time, the increase in the “c” parameter which represents three times the distance between the center of a brucite layer and the edge of the next layer can be explained by the increase in the quantity of La^{3+} ions in the brucite layers, which is characterized by a lower polarizing capacity than the other ions present. This weakens the interaction between hydroxides and carbonate ions, increasing this parameter [40]. For comparison, the unit cell parameters of hydrotalcite material with the same composition without lanthanum ($Ni_2Mg_4Al_2$) were calculated and added in Table 2. This composition has been prepared by conventional method ($Ni_2Mg_4Al_2$-C) as the sample (A) and under ultrasound ($Ni_2Mg_4Al_2$-US) in the same conditions as the sample (E). A slight difference is detected in the lattice parameters of these two samples, indicating that the variations observed in the hydrotalcite materials containing lanthanum prepared under sonication are probably due to better incorporation of lanthanum in the lamellar structure.

Finally, X-ray patterns of the calcined samples (Fig. 1-right) reveal the destruction of the hydrotalcite phases after calcination at 800 °C and the presence of the mixed oxides including MgO, NiO, $MgAl_2O_4$, and

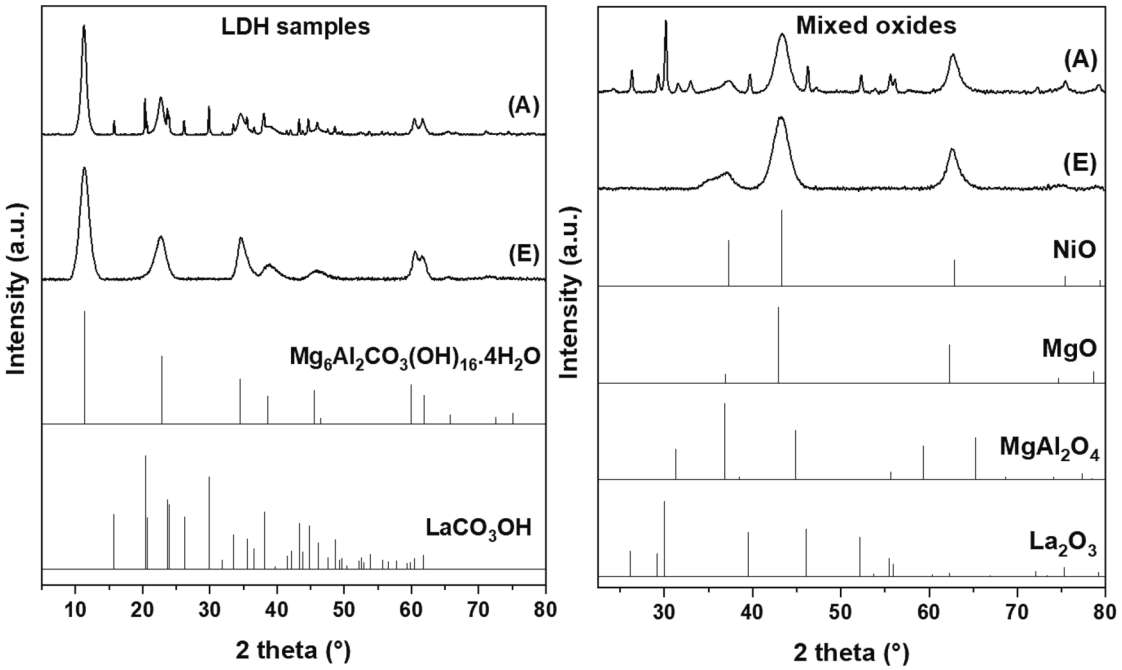

Fig. 1. XRD patterns of the LDH samples (left) and correspondent mixed oxides (right): Inputs A and E, ($Mg_6Al_2CO_3(OH)_{16}{\cdot}4H_2O$ JCPDS N° 22-0700; $LaCO_3OH$ JCPDS N° 49-0981; NiO JCPDS N° 44-1459; MgO JCPDS N° 43-1022; $MgAl_2O_4$ JCPDS N° 21-1152; La_2O_3 JCPDS N° 05-0602).

Table 2
Unit cell parameters of hydrotalcite materials for Inputs (A-G), and for $Ni_2Mg_4Al_2$ prepared by conventional method ($Ni_2Mg_4Al_2$-C) and under ultrasound ($Ni_2Mg_4Al_2$-US).

Input	*a* (Å)	*c* (Å)
A	3.051	23.087
B	3.056	23.441
C	3.061	23.491
D	3.065	23.512
E	3.069	23.577
F	3.067	23.568
G	3.062	23.508
$Ni_2Mg_4Al_2$-C	3.046	22.940
$Ni_2Mg_4Al_2$-US	3.048	22.993

La_2O_3 phases. This means a good incorporation of lanthanum on the material due to the mechanical effects of jets and shock waves issued from the acoustic cavitation phenomenon [31]. This species originates from the conversion of the isolated phases detected in the XRD profiles of the LDHs precursors by heat treatment [37]. The absence of these peaks points to the good dispersion of La_2O_3 in the mixed oxides resulting from the calcination of the LDHs precursors prepared by the ultrasonic-assisted method since lanthanum constitutes the lowest mass percentage of the elements present [39].

3.1.2. Infrared spectroscopy

The infrared spectroscopy was carried out to highlight the occurrence of layered double hydroxides characterized by M−OH bonds and interlayer anions especially carbonate vibrational modes (Fig. 2 and Fig. S2). Fig. 2 shows the selected infrared spectra of LDH reference (A) and UAS-LDH (E) as well as their mixed oxides A (MO) and E (MO), respectively. As expected, the characteristic Al-O-M vibrations bands (M = Ni, Mg, La) are observed in the range of 490–800 cm^{-1} interval [37,38]. The precursor A exhibits distinct broadened bands centered around 500–645 cm^{-1} and 645–780 cm^{-1} while for precursor E, these vibration bands appear to be merged. The first band presents two peaks at 562 cm^{-1} for A and E while the second peak is slightly shifted to a higher wavelength in the case of UAS-E compared to A (i.e. 606 cm^{-1} vs. 587 cm^{-1}, respectively). This suggests a difference in the geometric arrangement of Ni and La ions within the brucite layers, as confirmed by the ATR-FTIR spectra of the mixed oxides. Indeed, after thermal treatment, while the peak attributed to Al-O-Mg is located at 558 cm^{-1} for A (MO) and UAS-E (MO), the second peak assigned to Al-O-La and Al-O-Ni is shifted from 633 cm^{-1} to 652 cm^{-1} for A (MO) and UAS-E (MO), respectively [37]. Examination of the UAS spectra (Fig. S2) shows the same pattern of spectral shifts, which tends to demonstrate that they are caused by the possible insertion of lanthanum atoms induced under ultrasound.

For all samples, hydroxide vibrations at around 3200–3650 cm^{-1} are attributed to the stretching mode of water molecules and brucite layers while bands at 1595–1640 cm^{-1} are due to the OH bending mode of water in the interlayer space. For the latter, the mixed oxide UAS-E exhibits lower wavenumber compared to conventional A (MO) (i.e. 1598 cm^{-1} vs. 1632 cm^{-1}, respectively) probably due to bridging mode H_2O–CO_3^{2-}. For samples A and E, further OH bending vibrations are observed at the shoulder at 880–950 cm^{-1} (free water molecules), which disappear after calcination. Otherwise, all samples show characteristic peaks around 1360–1365 cm^{-1} (ν_3) and 855 cm^{-1} (ν_2) corresponding to interlayer carbonate ions as well as a component at 1480–1490 cm^{-1} ascribed to free lanthanum and sodium carbonates [38,39].

3.2. Textural investigation of materials

3.2.1. Morphological characterization

The average crystallite size, specific surface area (S_{BET}), porous volume (Vp) of the different hydrotalcite precursors, and correspondent mixed oxides are presented in Table 3. The sample prepared with the conventional co-precipitation method (input A) exhibits the largest crystallite size, lower S_{BET} areas, and reduced pore volume. The application of ultrasonic irradiation during the mixing stage (input B) leads to a consequent reduction of crystallite size combined with a significant increase in the specific surface area. The average crystallite size changes from 9.45 nm for A to 5.59 nm for B and the surface area of LDH precursor increases from 97 $m^2.g^{-1}$ to 120 $m^2.g^{-1}$ (inputs A and B, respectively). After calcination, mixed oxides retain the properties of the LDH precursors, particularly in regards to the pore volume (increase

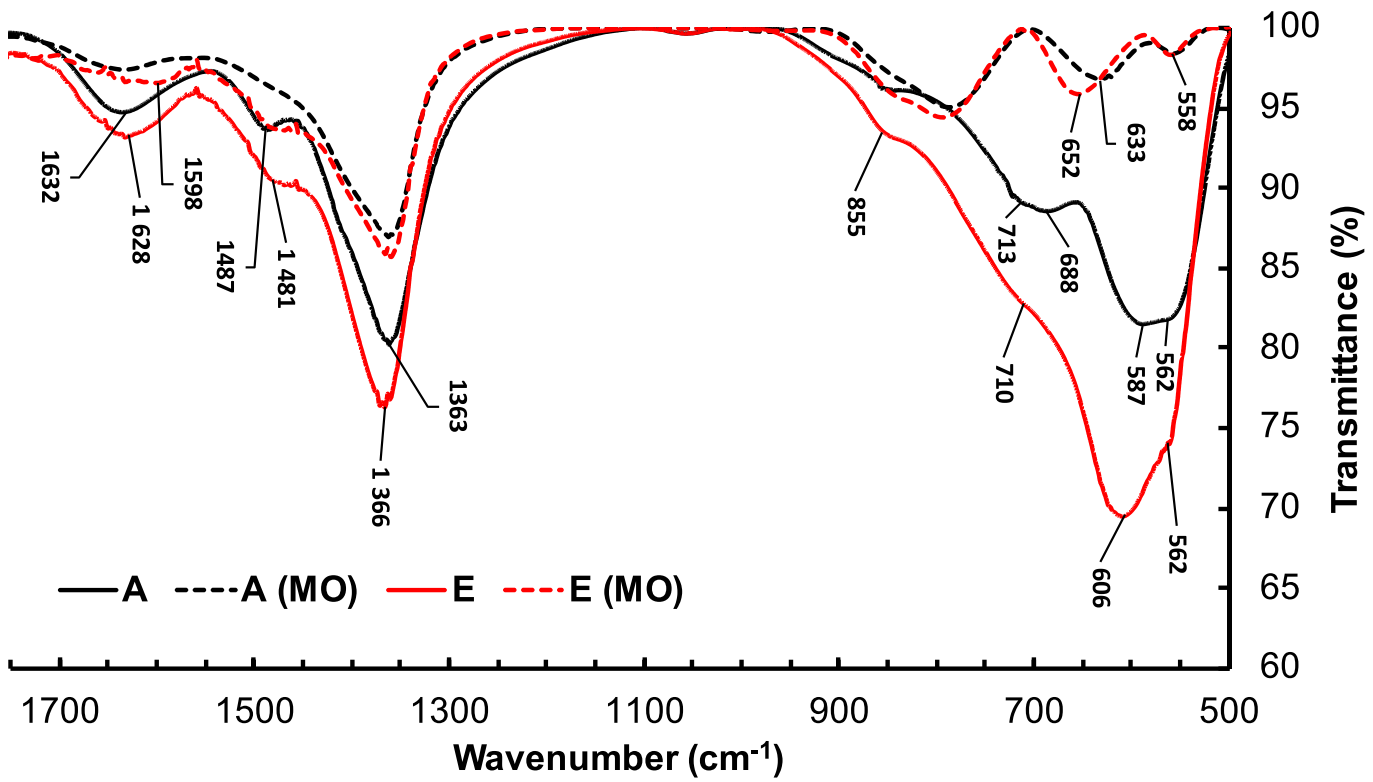

Fig. 2. ATR-FTIR spectra of LDH samples A and E and their mixed oxides A (MO) and E (MO).

Table 3
Crystallite size and the textural properties of LDHs and mixed oxides (MO).

Input	Average crystallite size (nm)	S_{BET} LDH ($m^2.g^{-1}$)	S_{BET} MO ($m^2.g^{-1}$)	Vp MO ($cm^3.g^{-1}$)	Pore diameter MO (nm)
A	9.45	97	157	0.48	13.72
B	5.99	120	172	0.75	15.68
C	5.59	115	170	0.71	14.21
D	5.18	136	183	0.89	15.74
E	4.88	140	187	1.11	17.78
F	4.87	137	180	0.82	15.68
G	4.65	123	153	0.87	18.28

from 0.48 to 0.78 $cm^3.g^{-1}$). This is because the application of ultrasounds leads to the production of smaller particles with a lower degree of agglomeration induced by violent collapsing bubbles, which prevents the aggregation and the growth of particles. Consequently, the decreased number of agglomerations induces an increase in the surface area. Next, the complete synthesis under ultrasound, including the aging step was carried out (input C). The results show a slight increase in particle size and no clear difference in textural properties compared to input B. As reported in the literature, the use of a short ultrasonic irradiation time during the precipitation step is recommended because when longer times are applied, particle growth takes place and larger particles are formed [40]. Sonication time was therefore reduced from 45 min (input C) to 15 min (input D), further improving the textural properties of the material are observed and are summarized in Table 3.

The temperature effect during sonication was then investigated and it has been reduced from 60 °C (input D) to 20 °C (input E) since raised temperature leads to a reduced sonochemical effect due to high vapor content cushions the implosion of the bubble. Thus, at room temperature, the average size of the nanocrystallites was further reduced to 4.88 nm, i.e. 6 % smaller than that synthesized at 60 °C (Input D) and over 50 % smaller than the conventional synthesis (Input A). The specific surfaces of samples D and E have been only slightly improved from 136 to 140 $m^2.g^{-1}$ and 183 to 187 $m^2.g^{-1}$ for precursor and mixed oxide, respectively. However, the pore volume of the mixed oxide obtained by ultrasound-assisted synthesis increased by more than 10 %, i.e. double the value obtained by the conventional synthesis method. Based on the optimal parameters of input E, the power density was then reduced to 180 $W.L^{-1}$ (input F) and 90 $W.L^{-1}$ (input G), respectively. We didn't observe any significant impact effect of the power density during UAS on the average crystallite size. The decrease of ultrasonic power at 180 $W.L^{-1}$ shows no influence on the average crystallite size while a slight decrease of the crystallite size from 4.87 to 4.65 nm at low powering (input G) is observed. Elsewhere, it is seen that by lowering ultrasonic power density to 180 $W.L^{-1}$, we observe a slight decrease in textural parameters which are close to those obtained at 60 °C (input D). Another decrease of power density to 90 $W.L^{-1}$ shows a significant decrease of S_{BET} from 180 to 153 $m^2.g^{-1}$.

The N_2 adsorption/desorption isotherms of mixed oxides are shown in Fig. 3. All samples exhibit an isotherm of type IV according to IUPAC classification, associated with the presence of mesoporous materials with H3 type characteristics which correspond to non-rigid aggregates of platelet-like particles forming slit-shaped pores [41]. The difference in isotherms between samples A and B indicates that the use of ultrasonic irradiations during the synthesis leads to changes in form shape and pore sizes. For samples B to D, there are no clear differences in the shapes of isotherm which shows that the conventional aging step has no remarkable effect on the textural properties of mixed oxides after the application of acoustic cavitation during the precipitation step.

Examination of the hysteresis loop for input D shows that the adsorption and desorption branches are almost parallel and narrower than for input E. This indicates the presence of pores more uniform in size and/or shape than the sample prepared at 60 °C which is consistent with the distribution of pores size (Fig. S3). Regarding the last three isotherms of mixed oxides issued from LDHs materials prepared by changing the power density, there is not a clear difference in the shape of these isotherms. However, the sample issued from the thermal treatment

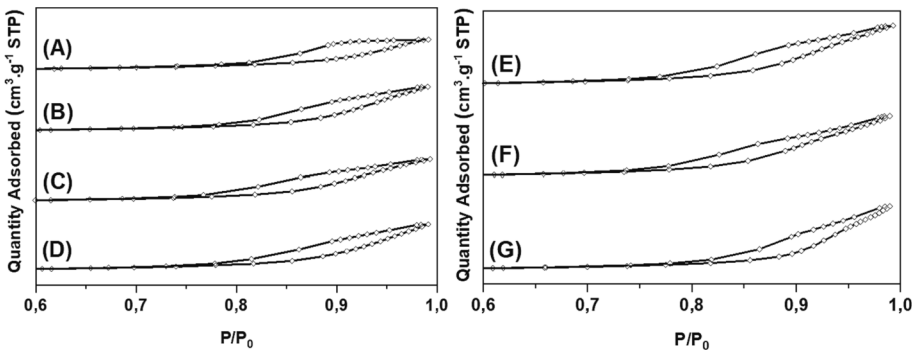

Fig. 3. N_2 adsorption/desorption isotherms of mixed oxides samples (inputs A to G).

of LDH material prepared by applying a power density of 180 $W.L^{-1}$ has a narrower distribution of the pore size. Moreover, the smaller pores size is observed for this sample.

3.2.2. SEM-EDX and S/TEM HAADF

Fig. 4 displays SEM images of materials from conventional and ultrasound-assisted syntheses (Inputs A and E), which reveal that LDHs are formed with a rosette morphology already observed in previous works [42,43]. The rosettes are constituted of platelets overlapping each other in different directions formed after the thermal treatment of the lamellar-like LDHs. The ultrasonic treatment induces the formation of smaller particles as observed in Fig. 4d which is a porous-like structure, by comparison with sample A (Fig. 4a) where a compact surface is observed. Consequently, the mixed oxides obtained in silent mode (Input A) (Fig. 4b) led to the coalescence of the platelets and formation of large regions with a smooth surface while the mixed oxides from sonicated material (Input E) (Fig. 4e) retained the plate-like morphology and leads to the formation of smaller aggregates or particles with smaller inter-particles pores. Moreover, there was detection of aggregates having flake-like morphology with irregular shapes and noticeable surface exfoliation. These observations reveal the presence of defects and distortions which are highly basic reactive sites that play an important role in applications involving carbon dioxide [44]. The comparison of representative images of SEM-EDX mapping on selected areas reveals that the application of ultrasounds leads to a homogeneous dispersion of La at the whole LDH structure (Fig. 4f), while conventional synthesis shows heterogeneous distribution and presence of agglomerates (Fig. 4c). This finding is consistent with the results obtained by XRD patterns of mixed oxides issued from calcination of sample A.

The morphology and the elemental distribution were analyzed by S/TEM coupled with EDSX analysis. Representative images are presented in Fig. 5, Fig. S.4, and S.5 in supplementary data. From the image statistics on the atomic distribution of La and Ni are recovered. In Fig. 5a and Fig. S4, for both A-LDH and A-OM phases, the structure looks compact with few apparent porosities, these results are coherent with the specific surfaces for these materials which are much lower than compared with US synthesis. For UAS-E, both the LDH and OM phases show a homogeneous distribution of filamentous structures, as shown in the HAADF images (Fig. 5d and Fig. S5), showing the beneficial effect of the US synthesis in the preparation of small-length filaments.

The insertion of a large quantity of La is observed for US synthesis for both LDH and OM phases. This is confirmed by elemental identification recovered from EDSX mappings (Fig. S6) where the presence of peaks corresponding to La is observed. From EDSX mapping, statistics presenting the average atomic % of La and Ni respectively are shown in Fig. 6. When ultrasonic synthesis is used, 8.11 % of La is inserted in the LDH structure (E-LDH) and 11.38 % in the OM structure (E-OM), whereas conventional co-precipitation synthesis allows only small incorporation of La with 2.45 % for LDH and 3.65 % for OM. This result is consistent with the measured lattice parameters of materials from ultrasonic-assisted synthesis, which showed an increase in the interlayer brucite distance more conducive to the insertion of lanthanum atoms. As

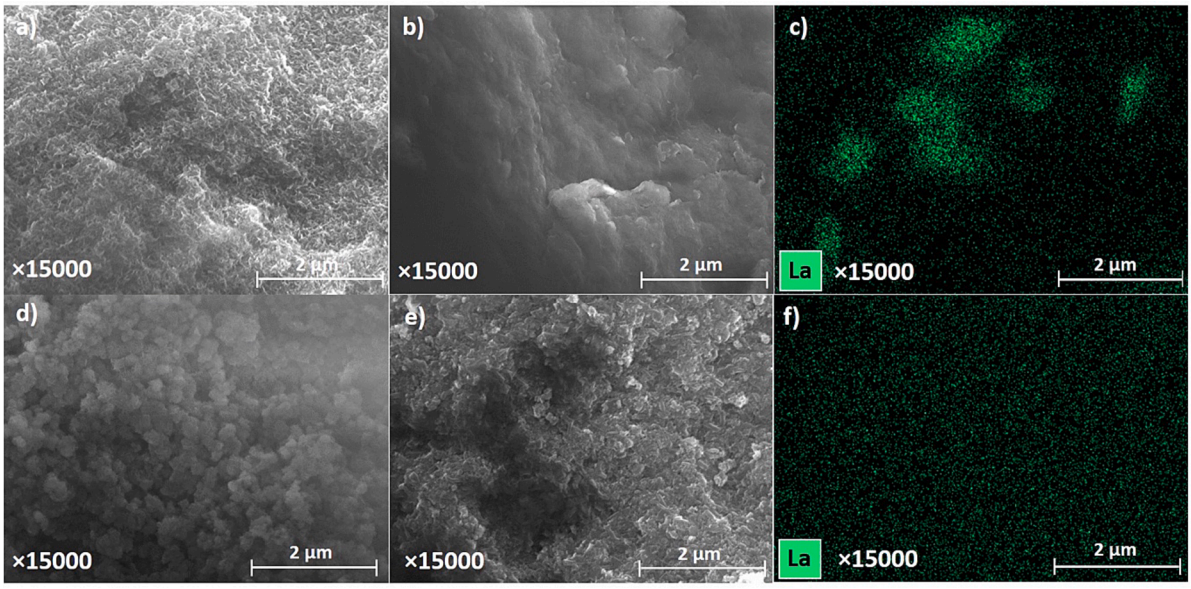

Fig. 4. SEM images of sample A (a: LDH, b: Mixed oxides, c: La-EDX mapping) and sample UAS-E (d: LDH, e: Mixed oxides, f: La-EDX mapping).

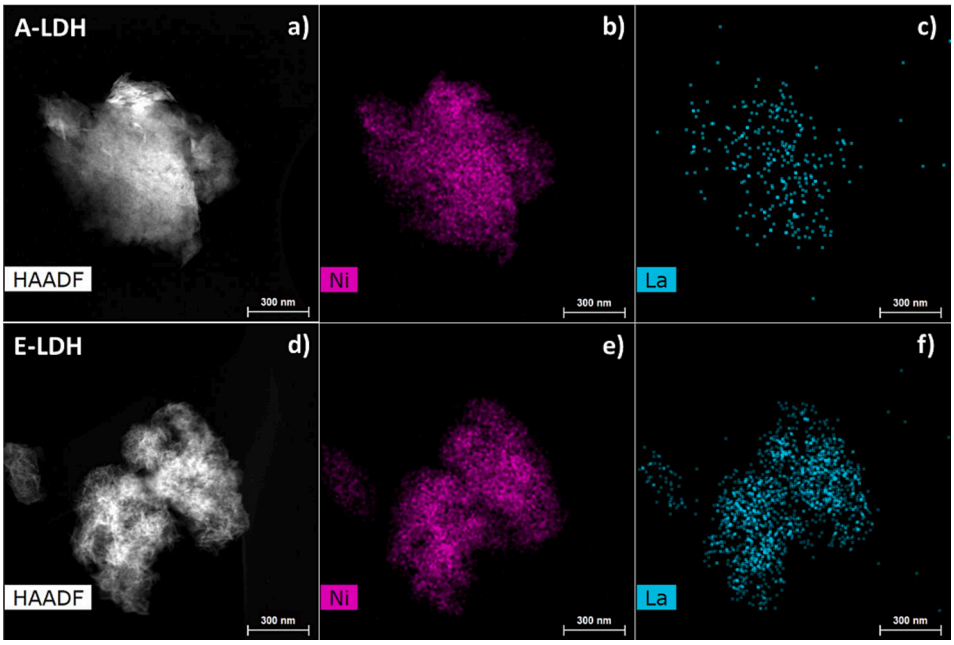

Fig. 5. S/TEM-HAADF (a, d) and EDSX mapping of Ni (b,e) and La (c, f) of A and E LDH materials.

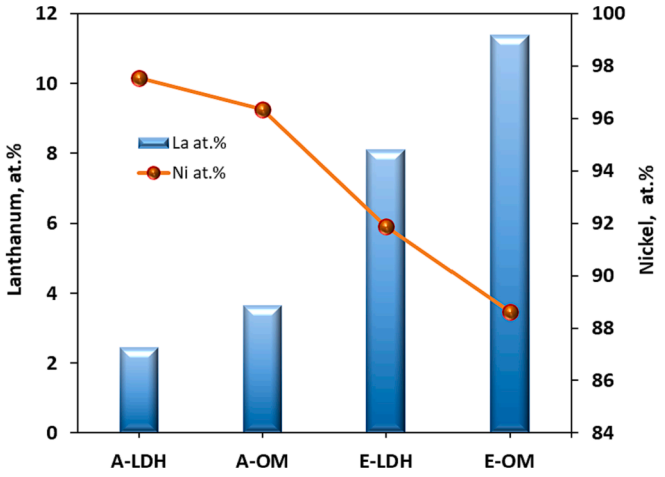

Fig. 6. Distribution of La at.% and Ni at.% from EDSX analysis.

a consequence, the proportion of nickel atoms decreases which suggests a possible substitution of nickel by lanthanum in brucite layers.

3.2.3. XPS analysis

XP spectra analysis is allowing to find out the composition at the surface of the solid, for the phases found at a maximum of 10 nm deep. In Fig. 7 are represented the spectra Ni 2p and La 3d of LDH materials A and E, respectively. The shape of the peaks BE is of Ni $2p_{3/2}$ BE of 854.3 eV and respectively for Ni $2p_{1/2}$ BE of 872 eV and 871.5 eV, together with the two satellites are associated with the presence of Ni(II) species from $Ni(OH)_2$ phase, which are typically found in LDH like materials [45]. Concerning the Lanthanum phases, hydroxides are also obtained for the LDH and their presence is confirmed by the spectra of La $3d_{5/2}$ (Fig. 7) with the BE of 833.4 eV, for La(III) species. As observed in Fig. 7 and Table S2, sample E is exposing more La on the surface of the LDH, by comparison with sample A and is proving the effectiveness of the US synthesis. (ΔE) is representing the binding energy difference between the La $3d_{5/2}$ peaks to identify the phase in which the lanthanum ions are present. Thus, the difference is 3.5 eV, which corresponds more closely to lanthanum present in carbonate form. In the sample prepared

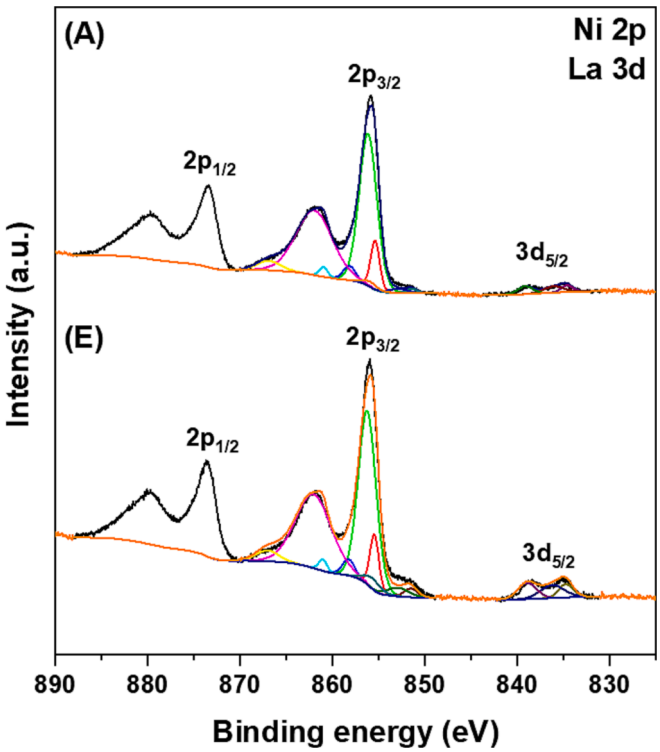

Fig. 7. XP spectra for the Ni 2p and La 3d of LDH materials A and E.

by the assistance of the acoustic cavitation phenomenon, the difference of 3.75 eV, corresponds to $La(OH)_3$ [46,47]. The binding energies of the other peaks reveal the presence of Ni, Mg, Al and La in the form of hydroxides, which is a confirmation of the formation of brucite layers containing metal hydroxides [48–50].

Furthermore, very interesting results are observed when looking at the O 1 s species (Fig. S7 and Table S1). Each species of oxygen is influencing the catalytic performances and their position on the solid and also their ratio is important to be identified. Thus, after the

deconvolution of the peaks of O 1 s, different species of oxygen are detected and are detailed in the following lines. At lower BE of 529.4 to 530.5 are identified species of surface lattice oxygen (O_{latt}) like O^{2-}, while the peak at the BE of 531.7 eV to 531.9 eV is attributed to the adsorbed oxygen species (O_{ads}), O_2^-, O_2^{2-} and O^-, respectively. Finally, the peak of the highest BE (533.3 eV) corresponds to the presence of oxygen species from water adsorbed and/or from hydroxyl groups. The ratio O_{ads}/O_{latt} was calculated based on the area of the fitted curves and is presented in Table S1. It is interesting to observe that when the US is used the O_{ads}/O_{latt} ratio is 0.8, while only 0,016 is obtained for conventional co-precipitation. Such results show that US may rise to materials with high oxygen mobility and also better adsorption of the reactive species which is beneficial for several catalytic applications [51,52].

4. Conclusion

In summary, the influence of ultrasonic parameters (power density, irradiation time, temperature) on the morphology of hydrotalcite and mixed oxides has been examined. One of the main aims of our work was to improve the insertion of La atom during LDH synthesis. The impact of ultrasounds on the synthesis procedure (during precipitation and aging steps) shows it has obtained a pure hydrotalcite phase. There are observed enhanced textural parameters (specific surface area and pore volume) and reduced crystallite size for materials derived from samples prepared under ultrasonic irradiations. Pure phases of LDHs are obtained with a drastic reduction of the total synthesis time, which was 45 min at room temperature for sample (E) versus 18 h at 60 °C for conventional co-precipitation (sample (A)). S/TEM-HAADF and EDXS mapping experiments have highlighted that ultrasonic synthesis leads to the production of LDH or MO with a homogenous distribution of the short filaments, together with a homogenous distribution of Ni, La, Mg, and Al nanoparticles over the porous and filamentous structure. As a consequence, the materials prepared with the assistance of acoustic cavitation are characterized by enhanced accessibility in comparison with more compact structures obtained by classical co-precipitation. We successfully proved that the synthesis under ultrasounds aims to incorporate ions like La more efficiently compared to the conventional synthesis, as proved by S/TEM-EDXS statistics. Furthermore, the ultrasonic-assisted method produced high-quality catalytic materials with enhanced oxygen mobility and better adsorption capacity as showed by XPS analysis due to a significantly high ratio O_{ads}/ O_{latt} on the surface of the sample E. This study shows that the Ni-Mg-Al-La catalyst combines the characteristics of nickel and lanthanum/magnesium which makes it a promising candidate for industrial dry reforming of biogas reaction.

CRediT authorship contribution statement

H. Kalawoun: Writing – original draft, Resources, Investigation. **C. Ciotonea:** Writing – review & editing, Supervision. **M. Marinova:** Investigation. **C. Gennequin:** Writing – review & editing, Supervision. **F. Delattre:** Writing – review & editing, Writing – original draft, Supervision, Methodology, Conceptualization.

Declaration of competing interest

The authors declare the following financial interests/personal relationships which may be considered as potential competing interests: Francois Delattre reports financial support was provided by University of the Littoral Opal Coast. If there are other authors, they declare that they have no known competing financial interests or personal relationships that could have appeared to influence the work reported in this paper.

Acknowledgments

The authors would like to thank the Université du Littoral Côte d'Opale (ULCO), the Pôle Métropolitain de la Côte d'Opale (PMCO), and the Communauté de Communes des Hauts de Flandre (CCHF) for funding this project. The authors thank also Mrs. Pardis Simon, engineer at Unité de Catalyse et Chimie du Solide (UCCS-UMR CNRS 8181), University of Lille for her contribution to XPS analyses.

Appendix A. Supplementary data

Supplementary data to this article can be found online at https://doi.org/10.1016/j.ultsonch.2024.106806.

References

[1] G. Mishra, B. Dash, S. Pandey, Layered double hydroxides: A brief review from fundamentals to application as evolving biomaterials, Appl. Clay Sci. 153 (Mar. 2018) 172–186, https://doi.org/10.1016/j.clay.2017.12.021.
[2] K.-H. Goh, T.-T. Lim, Z. Dong, Application of layered double hydroxides for removal of oxyanions: A review, Water Res. 42 (6–7) (Mar. 2008) 1343–1368, https://doi.org/10.1016/j.watres.2007.10.043.
[3] N. Dewangan, et al., Recent progress on layered double hydroxide (LDH) derived metal-based catalysts for CO2 conversion to valuable chemicals, Catal. Today 356 (Oct. 2020) 490–513, https://doi.org/10.1016/j.cattod.2020.06.020.
[4] V.K. Ameena Shirin, R. Sankar, A.P. Johnson, H.V. Gangadharappa, K. Pramod, Advanced drug delivery applications of layered double hydroxide, J. Controlled Release 330 (Feb. 2021) 398–426, https://doi.org/10.1016/j.jconrel.2020.12.041.
[5] Z.P. Xu, J. Zhang, M.O. Adebajo, H. Zhang, C. Zhou, Catalytic applications of layered double hydroxides and derivatives, Appl. Clay Sci. 53 (2) (Aug. 2011) 139–150, https://doi.org/10.1016/j.clay.2011.02.007.
[6] S. Elbasuney, Surface engineering of layered double hydroxide (LDH) nanoparticles for polymer flame retardancy, Powder Technol. 277 (Jun. 2015) 63–73, https://doi.org/10.1016/j.powtec.2015.02.044.
[7] X. He, X. Qiu, C. Hu, Y. Liu, Treatment of heavy metal ions in wastewater using layered double hydroxides: A review, J. Dispers. Sci. Technol. 39 (6) (Jun. 2018) 792–801, https://doi.org/10.1080/01932691.2017.1392318.
[8] B. Zümreoglu-Karan, A. Ay, Layered double hydroxides — multifunctional nanomaterials, Chem. Pap. 66 (1) (Jan. 2012) 1–10, https://doi.org/10.2478/s11696-011-0100-8.
[9] S. Nishimura, A. Takagaki, K. Ebitani, Characterization, synthesis and catalysis of hydrotalcite-related materials for highly efficient materials transformations, Green Chem. 15 (8) (2013) 2026, https://doi.org/10.1039/c3gc40405f.
[10] G. Fan, F. Li, D.G. Evans, X. Duan, Catalytic applications of layered double hydroxides: recent advances and perspectives, Chem. Soc. Rev. 43 (20) (Jul. 2014) 7040–7066, https://doi.org/10.1039/C4CS00160E.
[11] F. Cavani, F. Trifirb, A. Vaccari, Hydrotalcite-type anlonlc clays: preparation, properties and applications, p. 129, 1991, doi: 10.1016/0920-5861(91)80068-K.
[12] N. Chubar, et al., Layered double hydroxides as the next generation inorganic anion exchangers: Synthetic methods versus applicability, Adv. Colloid Interface Sci. 245 (Jul. 2017) 62–80, https://doi.org/10.1016/j.cis.2017.04.013.
[13] O.B. Belskaya, V.A. Likholobov, Mechanochemical Synthesis of Layered Double Hydroxides as a Promising Method for the Preparation of Adsorbents and Catalysts 63 (6) (2022) pp, https://doi.org/10.1134/S0023158422060015.
[14] J. He, M. Wei, B. Li, Y. Kang, D. G. Evans, X. Duan, Preparation of Layered Double Hydroxides, in: Layered Double Hydroxides, vol. 119, X. Duan and D. G. Evans, Eds., in Structure and Bonding, vol. 119. , Berlin/Heidelberg: Springer-Verlag, 2006, pp. 89–119. doi: 10.1007/430_006.
[15] M.R. Othman, Z. Helwani, Martunus, W.J.N. Fernando, Synthetic hydrotalcites from different routes and their application as catalysts and gas adsorbents: a review, Appl. Organomet. Chem. 23 (9) (Sep. 2009) 335–346, https://doi.org/10.1002/aoc.1517.
[16] E. Genty, et al., Co-Al Mixed Oxides Prepared via LDH Route Using Microwaves or Ultrasound: Application for Catalytic Toluene Total Oxidation, Catalysts 5 (2) (May 2015) 851–867, https://doi.org/10.3390/catal5020851.
[17] A. Pérez, J.-F. Lamonier, J.-M. Giraudon, R. Molina, S. Moreno, Catalytic activity of Co–Mg mixed oxides in the VOC oxidation: Effects of ultrasonic assisted in the synthesis, Catal. Today 176 (1) (Nov. 2011) 286–291, https://doi.org/10.1016/j.cattod.2010.11.088.
[18] M.N. Patil, A.B. Pandit, Cavitation – A novel technique for making stable nanosuspensions, Ultrason. Sonochem. 14 (5) (Jul. 2007) 519–530, https://doi.org/10.1016/j.ultsonch.2006.10.007.
[19] K. Prasad, D.V. Pinjari, A.B. Pandit, S.T. Mhaske, Synthesis of zirconium dioxide by ultrasound assisted precipitation: Effect of calcination temperature, Ultrason. Sonochem. 18 (5) (Sep. 2011) 1128–1137, https://doi.org/10.1016/j.ultsonch.2011.03.001.
[20] M. Espitia-Sibaja, M. Muñoz, S. Moreno, R. Molina, Effects of the cobalt content of catalysts prepared from hydrotalcites synthesized by ultrasound-assisted coprecipitation on hydrogen production by oxidative steam reforming of ethanol (OSRE), Fuel 194 (Apr. 2017) 7–16, https://doi.org/10.1016/j.fuel.2016.12.086.

[21] S. Zhao, et al., Enhancement effects of ultrasound assisted in the synthesis of NiAl hydrotalcite for carbonyl sulfide removal, Ultrason. Sonochem. 32 (Sep. 2016) 336–342, https://doi.org/10.1016/j.ultsonch.2016.04.001.
[22] H. Kalawoun, et al., Review on the contribution of ultrasounds in layered double hydroxides synthesis and in their performances, Comptes Rendus Chim. (2023), https://doi.org/10.5802/crchim.249.
[23] E. Dahdah, J. Estephane, C. Gennequin, A. Aboukaïs, S. Aouad, E. Abi-Aad, Effect of La promotion on Ni/Mg-Al hydrotalcite derived catalysts for glycerol steam reforming, J. Environ. Chem. Eng. 8 (5) (Oct. 2020) 104228, https://doi.org/10.1016/j.jece.2020.104228.
[24] H. Kalawoun, M. Chaghouri, C. Ciotonea, C. Gennequin, F. Delattre, Mixed oxide preparation by ultrasonic assisted method. Toward hydrogen production via CO $_2$ reforming of methane, in: 2022 13th International Renewable Energy Congress (IREC), Hammamet, Tunisia: IEEE, Dec. 2022, pp. 1–5. doi: 10.1109/IREC56325.2022.10002137.
[25] A.F. Lucrédio, J.D.A. Bellido, E.M. Assaf, Effects of adding La and Ce to hydrotalcite-type Ni/Mg/Al catalyst precursors on ethanol steam reforming reactions, Appl. Catal. Gen. 388 (1–2) (Nov. 2010) 77–85, https://doi.org/10.1016/j.apcata.2010.08.026.
[26] J. Zhang, N. Zhao, W. Wei, Y. Sun, Partial oxidation of methane over Ni/Mg/Al/La mixed oxides prepared from layered double hydrotalcites, Int. J. Hydrog. Energy 35 (21) (Nov. 2010) 11776–11786, https://doi.org/10.1016/j.ijhydene.2010.08.025.
[27] Z. Bian, S. Das, M.H. Wai, P. Hongmanorom, S. Kawi, A Review on Bimetallic Nickel-Based Catalysts for CO $_2$ Reforming of Methane, ChemPhysChem 18 (22) (Nov. 2017) 3117–3134, https://doi.org/10.1002/cphc.201700529.
[28] R. Martınez, E. Romero, C. Guimon, and R. Bilbao, "CO2 reforming of methane over coprecipitated Ni–Al catalysts modified with lanthanum," 2004, doi: 10.1016/j.apcata.2004.06.017.
[29] A. Serrano-Lotina, A.J. Martin, M.A. Folgado, L. Daza, Dry reforming of methane to syngas over La-promoted hydrotalcite clay-derived catalysts, Int. J. Hydrog. Energy 37 (17) (Sep. 2012) 12342–12350, https://doi.org/10.1016/j.ijhydene.2012.06.041.
[30] H. Liu, La-promoted Ni-hydrotalcite-derived catalysts for dry reforming of methane at low temperatures, 2016, doi: 10.1016/j.fuel.2016.05.073.
[31] O. R. Macedo Neto, N. F. P. Ribeiro, C. A. C. Perez, M. Schmal, M. M. V. M. Souza, Incorporation of cerium ions by sonication in Ni–Mg–Al layered double hydroxides, Appl. Clay Sci., vol. 48, no. 3, pp. 542–546, Apr. 2010, doi: 10.1016/j.clay.2010.02.015.
[32] J. de Souza Rossi et al., Effect of lanthanide ion doping on Mg−Al mixed oxides as active acid−base catalysts for fatty acid ethyl ester synthesis, Renew. Energy, vol. 133, pp. 367–372, Apr. 2019, doi: 10.1016/j.renene.2018.10.038.
[33] J. Abou Rached et al., Effects of cerium and lanthanum on Ni-based catalysts for CO2 reforming of toluene, J. Environ. Chem. Eng., vol. 6, no. 4, pp. 4743–4754, Aug. 2018, doi: 10.1016/j.jece.2018.06.054.
[34] C. Gennequin, et al., Co–Mg–Al oxides issued of hydrotalcite precursors for total oxidation of volatile organic compounds. Identification and toxicological impact of the by-products, Comptes Rendus Chim. 13 (5) (May 2010) 494–501, https://doi.org/10.1016/j.crci.2010.01.001.
[37] N.T. McDevitt, W.L. Baun, Infrared absorption study of metal oxides in the low frequency region (700–240 cm-1), Spectrochim. Acta 20 (1964) 799–808, https://doi.org/10.1016/0371-1951(64)80079-5.
[38] D.M. Bezerra, Structural, vibrational and morphological properties of layered double hydroxides containing Ni2+, Zn2+, Al3+ and Zr4+ cations, Mater. Charact. (2017), https://doi.org/10.1016/j.matchar.2017.01.015.
[39] J.T. Kloprogge, D. Wharton, L. Hickey, R.L. Frost, Infrared and Raman study of interlayer anions CO32–, NO3–, SO42– and ClO4– in Mg/Al- hydrotalcite, Am. Mineral. 87 (2002) 623–629, https://doi.org/10.2310/am-2002-5-604.
[40] T. Hosseini, M. Haghighi, H. Ajamein, Fuel cell-grade hydrogen production from methanol over sonochemical coprecipitated copper based nanocatalyst: Influence of irradiation power and time on catalytic properties and performance, Energy Convers. Manag. 126 (Oct. 2016) 595–607, https://doi.org/10.1016/j.enconman.2016.07.056.
[41] G. Leofanti, M. Padovan, G. Tozzola, B. Venturelli, Surface area and pore texture of catalysts, Catal. Today 41 (1–3) (May 1998) 207–219, https://doi.org/10.1016/S0920-5861(98)00050-9.
[42] Q. Wang, et al., Morphology and composition controllable synthesis of Mg–Al–CO3 hydrotalcites by tuning the synthesis pH and the CO2 capture capacity, Appl. Clay Sci. 55 (Jan. 2012) 18–26, https://doi.org/10.1016/j.clay.2011.07.024.
[43] A. Faour, V. Prévot, C. Taviot-Gueho, Microstructural study of different LDH morphologies obtained via different synthesis routes, J. Phys. Chem. Solids 71 (4) (Apr. 2010) 487–490, https://doi.org/10.1016/j.jpcs.2009.12.018.
[44] M. Muñoz, S. Moreno, R. Molina, Oxidative steam reforming of ethanol (OSRE) over stable NiCo–MgAl catalysts by microwave or sonication assisted coprecipitation, Int. J. Hydrog. Energy 42 (17) (Apr. 2017) 12284–12294, https://doi.org/10.1016/j.ijhydene.2017.03.090.
[45] T.S. Munonde, H. Zheng, The impact of ultrasonic parameters on the exfoliation of NiFe LDH nanosheets as electrocatalysts for the oxygen evolution reaction in alkaline media, Ultrason. Sonochem. 76 (Aug. 2021) 105664, https://doi.org/10.1016/j.ultsonch.2021.105664.
[46] A.B. Yousaf, M. Imran, M. Farooq, P. Kasak, Interfacial Phenomenon and Nanostructural Enhancements in Palladium Loaded Lanthanum Hydroxide Nanorods for Heterogeneous Catalytic Applications, Sci. Rep. 8 (1) (Mar. 2018) 4354, https://doi.org/10.1038/s41598-018-22800-0.
[47] D. Wu, Y. Zhan, J. Lin, Z. Zhang, B. Xie, Contrasting effect of lanthanum hydroxide and lanthanum carbonate treatments on phosphorus mobilization in sediment, Chem. Eng. J. 427 (Jan. 2022) 132021, https://doi.org/10.1016/j.cej.2021.132021.
[48] M. Richetta, et al., Surface spectroscopy and structural analysis of nanostructured multifunctional (Zn, Al) layered double hydroxides: XPS and UPS investigation of nanostructured multifunctional LDH, Surf. Interface Anal. 48 (7) (Jul. 2016) 514–518, https://doi.org/10.1002/sia.5973.
[49] S. Ardizzone, C.L. Bianchi, M. Fadoni, B. Vercelli, Magnesium salts and oxide: an XPS overview, Appl. Surf. Sci. 119 (3–4) (Oct. 1997) 253–259, https://doi.org/10.1016/S0169-4332(97)00180-3.
[50] S.-T. Lin, H.N. Tran, H.-P. Chao, J.-F. Lee, Layered double hydroxides intercalated with sulfur-containing organic solutes for efficient removal of cationic and oxyanionic metal ions, Appl. Clay Sci. 162 (Sep. 2018) 443–453, https://doi.org/10.1016/j.clay.2018.06.011.
[51] J. Cheng, J. Yu, X. Wang, L. Li, J. Li, Z. Hao, Novel CH4 Combustion Catalysts Derived from Cu-Co/X-Al (X) Fe, Mn, La, Ce) Hydrotalcite-like Compounds, Energy Fuels 22 (2008) 2131–2137, https://doi.org/10.1021/ef8000168.
[52] J.-R. Li, F.-K. Wang, C. He, C. Huang, H. Xiao, Catalytic total oxidation of toluene over carbon-supported Cu-Co oxide catalysts derived from Cu-based metal organic framework, Powder Technol. 363 (2020) 95–106, https://doi.org/10.1016/j.powtec.2019.12.060.

Further reading

[35] X. Yu, N. Wang, W. Chu, M. Liu, Carbon dioxide reforming of methane for syngas production over La-promoted NiMgAl catalysts derived from hydrotalcites, Chem. Eng. J. 209 (Oct. 2012) 623–632, https://doi.org/10.1016/j.cej.2012.08.037.
[36] R. Bîrjega, O.D. Pavel, G. Costentin, M. Che, E. Angelescu, Rare-earth elements modified hydrotalcites and corresponding mesoporous mixed oxides as basic solid catalysts, Appl. Catal. Gen. 288 (1–2) (Jul. 2005) 185–193, https://doi.org/10.1016/j.apcata.2005.04.030.